

An Extreme Cold-Air Outbreak over the Labrador Sea: Roll Vortices and Air–Sea Interaction

IAN A. RENFREW AND G. W. K. MOORE

Department of Physics, University of Toronto, Toronto, Ontario, Canada

(Manuscript received 16 March 1998, in final form 8 December 1998)

ABSTRACT

Observational data from two research aircraft flights are presented. The flights were planned to investigate the air–sea interaction during an extreme cold-air outbreak, associated with the passage of a synoptic-scale low pressure system over the Labrador Sea during 8 February 1997. This is the first such aircraft-based investigation in this remote region. Both high-level dropsonde and low-level flight-level data were collected. The objectives were twofold: to map out the structure of the roll vortices that cause the ubiquitous cloud streets seen in satellite imagery, and to estimate the sensible and latent heat fluxes between the ocean and atmosphere during the event. The latter was achieved by a Lagrangian analysis of the flight-level data. The flights were part of the Labrador Sea Deep Convection Experiment, investigating deep oceanic convection, and were planned to overpass a research vessel in the area.

The aircraft-observed roll vortices had a characteristic wavelength of 4–5 km, particularly evident in the water vapor signal. Unlike observations of roll vortices in other regions, a roll signature was absent from the temperature data. Analysis of satellite imagery shows the cloud streets had a characteristic wavelength of 7–10 km, indicating a multiscale roll vortex regime. There was a dramatic deepening of the boundary layer with fetch, and also with time. Off the ice edge, surface sensible heat fluxes of 500 W m^{-2} and surface latent heat fluxes of 100 W m^{-2} were measured, with uncertainties of $\pm 20\%$. The very cold air is thought to be responsible for the unusually high Bowen ratio observed.

1. Introduction

Cloud streets, illustrated so beautifully by satellite imagery such as Fig. 1, are a ubiquitous feature of cold-air outbreaks at high latitudes. Their existence suggests that the shallow convection they represent is organized into two-dimensional streets by “roll vortices,” aligned approximately in the direction of the low-level wind. Etling and Brown (1993) and Atkinson and Zhang (1996) review roll vortices and shallow convection, summarizing observational, theoretical, modeling, and laboratory studies. The observational studies cover a range of meteorological conditions and utilize a variety of observing platforms. For example, observations from fixed towers (LeMone 1973), satellite (Walter 1980; Miura 1986), aircraft (Walter and Overland 1984; Brümmer et al. 1985; Hein and Brown 1988; Chou and Ferguson 1991), airborne lidar (Atlas et al. 1986), radar (Kelly 1984; Kristovich 1993; Weckworth et al. 1997), and synthetic aperture radar (Alpers and Brummer 1994) have been studied. A variety of horizontal scales, aspect

ratios, lifetimes, and synoptic environments have been found. Indeed it is now clear that no one process is responsible for the medley of roll vortices observed; rather a number of mechanisms are at work in different locations and in different conditions. These include an “inflection point” instability of the cross-roll boundary layer wind profile, which results in two-dimensional rolls with aspect ratios around 2–3 (Faller and Kaylor 1966; Lilly 1966; Brown 1970, 1972), or a buoyancy-driven thermal instability, driven by shallow convection and oriented in the direction of the mean vertical shear (Asai 1970; Kuettner 1959, 1971). These basic mechanisms can occur together and will also be modified by the boundary layer environment and interactions with topography, gravity waves, or mesoscale flow variations (e.g., LeMone 1973; Clark et al. 1986; Mourad and Brown 1990; Weckworth et al. 1997).

This study adds to the limited collection of in situ roll vortex data and provides the precedent of a location never before investigated by aircraft, the Labrador Sea. The Labrador Sea is currently the subject of intense study as it is one of very few regions in the world where an overturning of the whole ocean column occurs (Killworth 1983). This is a keystone in the ocean’s thermohaline circulation and, hence, an important component in the earth’s climate system. To investigate this

Corresponding author address: Dr Ian Renfrew, Ice and Climate Division, British Antarctic Survey, High Cross, Madingley Road, Cambridge CB3 0ET, United Kingdom.
E-mail: I.Renfrew@bas.ac.uk



FIG. 1. AVHRR infrared satellite image of the Labrador Sea region from NOAA-I2 at 1119 UTC 8 Feb 1997. A low pressure system fills the image, with high cloud to the north and west. Within the low there are a number of convective cloud vortices, and a convective cloud band curving northwest-southeast. There are cloud streets over the marginal ice zone and the ice-free Labrador Sea in the cold cyclonic flow to the south. Sea ice contours of 50% and 75% concentration, as derived from the SSM/I passive microwave sensor, are overlaid. The three stacks of the low-level portion of the flight are marked 1, 2, 3; the end points of the dropsonde run are marked as large dots; and the location of the R/V *Knorr* by a K. The AVHRR data is from the University of Toronto receiving system.

process a major research program has been launched: the Labrador Sea Deep Convection Experiment (Lab Sea Group 1998). This has the aim “to improve our understanding of the convective process in the ocean, and hence the fidelity of its parametric representation in large-scale ocean models, through a combination of meteorological and oceanographic field observations, laboratory studies, theory, and modeling.” During Feb-

ruary and March 1997 there was a 40-day cruise by the R/V *Knorr* in the Labrador Sea. It carried out hydrographic surveys, launched oceanographic instruments, and had a number of meteorological instruments on board. We also had at our disposal two C-130 aircraft of the U.S. Air Force Reserve 53d Squadron—the “Hurricane Hunters.” To aid the planning of intensive observing periods and ship operations a meteorological

forecast model, the U.S. Navy's Coupled Ocean–Atmosphere Mesoscale Prediction System (COAMPS; see Hodur 1997), was run over a Labrador Sea domain especially for the project. Twice-daily forecasts out to 36 h with nonstandard fields such as 10-m winds and surface fluxes were available at 1-h intervals. These data were to prove invaluable in the planning process, as detailed in Renfrew et al. (1999).

The exchange of heat and moisture across the air–sea boundary is the primary forcing for open ocean convection (Killworth 1983). In particular, the cooling and salinization of the ocean surface during a cold-air outbreak leads to an increase in density of the surface waters, and so may trigger convective overturning, given suitable oceanic preconditioning into a weakly stratified state.

This study concentrates on one cold-air outbreak during the ocean convection season, that of 8 February 1997. The primary aircraft flight was planned to allow Lagrangian estimates of the surface fluxes, by attempting to “follow an air parcel” from over the sea ice to over the open ocean. The aircraft instrumentation was not able to measure surface fluxes explicitly—only estimates of the surface fluxes were possible after a number of approximations and assumptions. In this respect, this study falls short of recent state-of-the-art atmospheric boundary layer (ABL) budget studies such as those of Grossman and Betts (1990), Bretherton and Pincus (1995), or Brümmer (1997). What makes this study of vital interest is the quality and temporal extent of atmospheric measurements made in an isolated location that is currently the object of intense scientific inquiry. Indeed, the location of the flight covered the main area of expected oceanic convection (Lab Sea Group 1998) and also overpassed the R/V *Knorr*, allowing a comparison with the ship-based data.

The purpose of the flights was thus twofold: to investigate the structure of the roll vortices, and to estimate the surface sensible and latent heat fluxes. In section 2 of this study the synoptic picture is briefly described. In section 3 the flight plan is detailed, and in section 4 cross sections at two stages of the cold-air outbreak are presented. Section 5 focuses on examining the roll vortices using flight-level and satellite data. Section 6 quantifies and discusses the air–sea interaction, before the conclusions are presented in section 7.

2. Synoptic situation

On 6 February 1997 a low pressure system moved from the Great Lakes region of North America toward Newfoundland, deepened rapidly as it reached the North Atlantic, and then tracked toward Greenland. At the same time a smaller low pressure system drifted south from the Arctic, via Hudson Strait, into the northern Labrador Sea. On 7 February the northward moving low split around the coastal mountains of Greenland, forming an eastern low center and a western low center. The

western low then merged with the smaller Arctic system, the result being a large low pressure system covering much of the Labrador Sea region on 8 February 1997. Figure 2 shows the sea level pressure and total surface heat fluxes at 1200 UTC 8 February from the COAMPS model analysis. The analyzed cyclone in the Labrador Sea had a low pressure center of 984 mb located at 63°N, 58°W. It was associated with a substantial height anomaly and a vorticity maximum at the 500-mb level. The satellite image in Fig. 1 focuses on the central portion of the synoptic low. The high clouds to the north and west are associated with the low's warm sector being wrapped around cyclonically. In the cold air to the south, the shallow clouds are organized into cloud streets, changing to a cellular pattern farther downstream. There are two small convective cloud vortices off the ice edge (at 60° and 58°N), and a convective cloud band oriented northwest–southeast, embedded within the low pressure system.

A flight was planned into the westerly (offshore) flow at around 55°N (Fig. 1). The expected situation fulfilled all our criteria for a Labrador Sea Experiment boundary layer flight: very cold air, strong low-level winds perpendicular to the ice edge with relatively low curvature, and peak surface heat fluxes forecast over an area of known reduced oceanic stability (Fig. 2 and Lab Sea Group 1998). The real-time availability of COAMPS hourly forecasts of surface winds and fluxes allowed the flights to be timed to capture these peak fluxes, as well as the evolution of the atmospheric boundary layer.

3. The flight plan

The C-130 aircraft were equipped with dropsondes and flight-level sensors for temperature, dewpoint temperature, horizontal winds, and pressure. The temperature was measured using a Rosemount thermistor, the dewpoint temperature by an Edgetech 137-C3 hygrometer, the winds via air speed and navigational measurements, and the pressure by an AirPressure barometer. Flight-level data were sampled at 60 Hz but unfortunately only recorded at 1 Hz and did not include vertical velocity. This meant an eddy correlation measurement of surface fluxes was not possible. To circumvent this limitation a novel Lagrangian flight plan was designed. The plan allowed a sampling of the roll vortices in cross section, as well as approximately “following an air parcel” downstream. Measurements of heat and moisture changes in the air parcel would then allow an estimate of surface fluxes. The Lagrangian nature of the plan was an adaption of that used by, for example, Grossman and Betts (1990) and Bretherton and Pincus (1995). Figure 3 shows a schematic of the plan. First a high-level (around 500 mb) dropsonde leg was flown, perpendicular to the ice edge and approximately 180° from the low-level wind direction. The low-level wind direction was taken from model forecasts and modified in flight from the dropsonde data. The plane then spiraled down

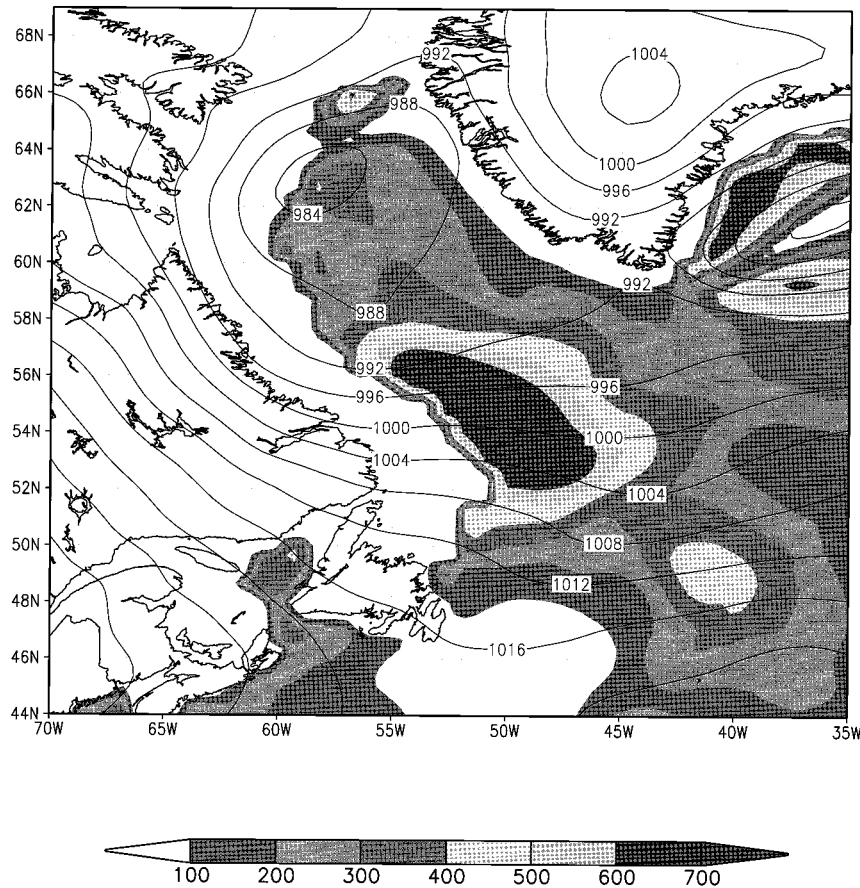


FIG. 2. Sea level pressure contours (4-mb interval) and total heat flux shading (W m^{-2}) for 1200 UTC 8 Feb 1997 from the operational COAMPS model analysis.

to low levels to fly a series of stacks approximately perpendicular to the mean low-level wind direction. Each stack consisted of three legs (one on top of the other) at approximately 170, 300, and 450 m above mean sea level and around 85 km in length. A diagonal leg (at 450 m) was then flown to the start of the next stack. The positions of the stacks were planned, using sea ice maps from the Canadian Ice Service, to have stack 1 over the sea ice, stack 2 over the marginal ice zone (MIZ), and stacks 3 and 4 over the open ocean. A sea ice mask, calculated from passive microwave data, has been overlaid on Fig. 1. The ice concentrations are over 75% at stack 1, and between 50% and 75% at stack 2. Note that the cloud streets start over the MIZ, rather than at the “ice edge” as often supposed. The length of the stacks were calculated to make the flight plan Lagrangian: to be precise we attempted to sample the same air parcels at each height, for each stack. Unfortunately only three of the planned four stacks were flown. The plane had some trouble in one engine during the low-level portion of the flight, forcing an early retreat from this remote location.

4. Cross sections of the cold-air outbreak

Figure 4 shows a cross section at 1200 UTC 8 February 1997 approximately perpendicular to the ice edge (see Fig. 1) of (a) equivalent potential temperature (θ_e), and (b) specific humidity (q). The plots are obtained from the dropsonde data via a one-dimensional smoothing spline algorithm in the vertical (Reinsch 1967; Thiébaux and Pedder 1987), followed by linear interpolation in the horizontal. The smoothing spline algorithm allows for a small amount of noise in the data, which can be set to the accuracy of the instruments; in this case set at 0.3°C for temperature, 5% for relative humidity, 5° for wind direction, and 0.5 m s^{-1} for wind speed (J. Talbot 1997, personal communication). The sondes measured pressure, temperature, and relative humidity every 10 s (equivalent to every 4–8 mb), and wind speed and direction every 30 s (every 10–20 mb). In the vertical, the data are approximated on a 10-mb grid, so retaining features on this scale. In the horizontal, the location of the sondes are marked by tabs at the top of the figure, and the data have been interpolated onto a 0.5° longitude grid.

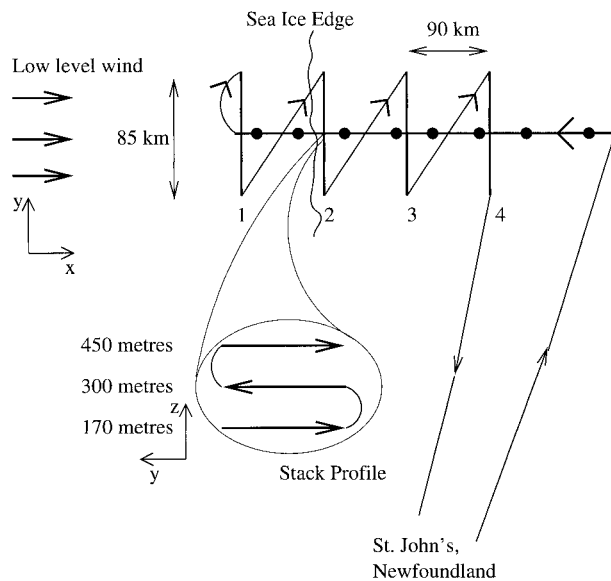


FIG. 3. A schematic of the planned flight pattern, showing the dropsonde leg (dotted), the low-level stacks labeled 1–4, and the three legs flown at each stack position. Due to engine problems stack 4 was not flown.

A deepening of the boundary layer with downstream distance (to the east) is clearly illustrated in Fig. 4a. Over the sea ice (to the west) the boundary layer is generally of neutral stability, with a strong inversion at the ABL top. Moving downstream (to the east) there is a tight horizontal gradient of θ_e between 52° and 51°W , over and at the edge of the MIZ where one would expect the greatest air–sea temperature differences. The boundary layer becomes conditionally unstable (i.e., unstable to moist convection) around 51°W . These changes correspond to a progression from solid ice cover to the west of the cross section, into the marginal ice zone, then to open ocean conditions to the east (Fig. 1). Figure 4b shows water vapor (as specific humidity q) for the same cross section and shows a moistening of the boundary layer with fetch. There is a sharp horizontal gradient of q concentrated between 52° and 50°W , at the edge of the MIZ.

A dashed line in Fig. 4a contours the $N_s^2 = 1 \times 10^{-4} \text{ s}^{-1}$ line, where N_s^2 is the moist Brunt–Väisälä frequency [$N_s^2 = (g/\theta_e)(\partial\theta_e/\partial z)$]. The continuous N_s^2 line, at the sharp increase in θ_e , is taken as defining the boundary layer top, or inversion height (z_i). This varies from 890 mb up to 780 mb from west to east, corresponding to z_i rising from approximately 850 to 1800 m over the 380-km cross section. This dramatic rise in boundary layer height, combined with the warming with fetch, is indicative of large surface sensible heat fluxes warming the boundary layer. This is discussed in more detail in section 6.

Figure 5 shows a cross section of the wind components normal (approximately cross roll) and parallel (approximately along roll) to the dropsonde leg. There is

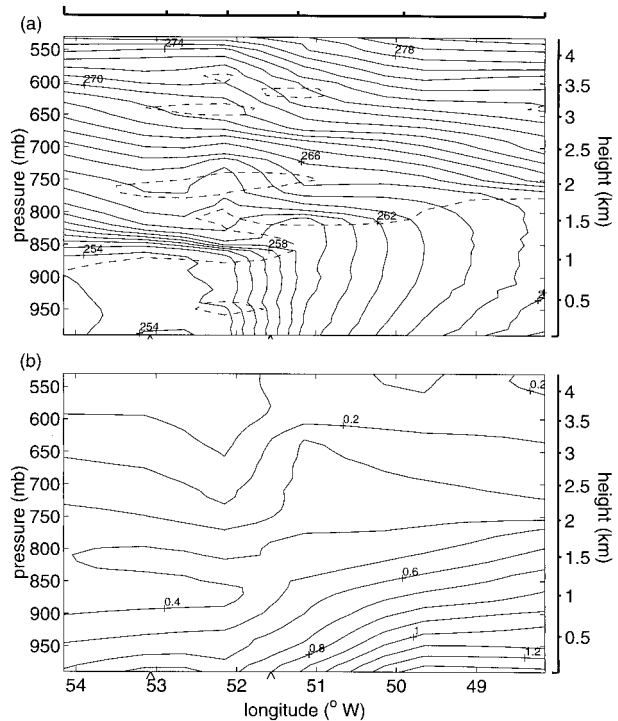


FIG. 4. Cross sections of (a) equivalent potential temperature (θ_e) and (b) specific humidity (q) from the 1200 UTC dropsonde run. The sections are approximately 380 km in length from west to east. A height scale calculated hydrostatically for the mean temperature of the section is shown on the right. The locations of the sondes are indicated by tabs at the top of the figure. The contour intervals are 1 K and 0.1 g kg^{-1} , respectively. Note stacks 2 and 3 are located at approximately 53.1° and 51.6°W on this section, as marked by the “^” symbols. The marginal ice zone is between 54° and 52°W . The height of the boundary layer is marked by the $N_s^2 = 1 \times 10^{-4} \text{ s}^{-1}$ contour shown as a dashed line on the θ_e cross section. This also highlights what may be an internal gravity wave at 52°W .

a pronounced jet just above the ABL top with winds up to 24 m s^{-1} in the jet core. The jet has a signature in both wind components and represents a backing of the wind to the south in the jet core. The backing is consistent with the jet being in thermal wind balance with the tight horizontal temperature gradient across the MIZ (Fig. 4a), although we should note that the downstream component of the jet is somewhat larger than might be expected by thermal wind balance. In general in the boundary layer, winds are between 10 and 14 m s^{-1} in the downstream direction and much smaller in the cross-stream direction.

The same dropsonde cross section was flown as part of a separate aircraft mission 10 h earlier to the main flight, starting at 0200 UTC 8 February 1997. These earlier dropsonde data allow a rare opportunity to study the temporal evolution of the marine boundary layer during an extreme cold air outbreak. Figure 6a shows θ_e and Fig. 6b q from this earlier run. At this stage of the cold air outbreak the horizontal gradient in θ_e is reduced, with warmer θ_e air at the western side, and

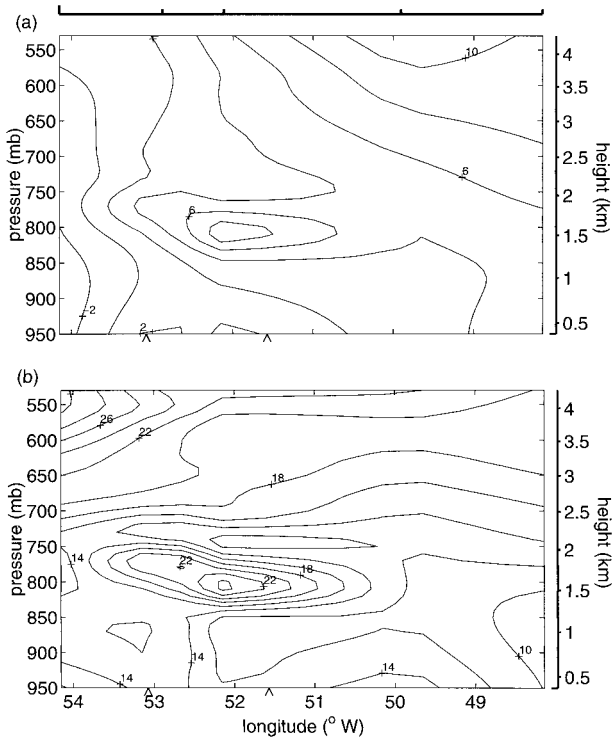


FIG. 5. Cross sections of (a) normal wind component and (b) parallel wind component from the 1200 UTC dropsonde run. Dropsonde and stack locations are marked as for Fig. 4. The contour interval is 2 m s^{-1} . A strong jet near the ice edge is evident around the 800-mb level.

roughly the same θ_e at the eastern side, compared to the 1200 UTC cross section. The air is also more moist at this time, with again a horizontal gradient in q from west to east. The ABL top rises from around 890 to 820 mb, corresponding to an inversion height rising from approximately 850 to 1500 m, over the 380-km section. The boundary layer over the open ocean is unstable to moist convection. The winds at the earlier time (not shown) are more uniform at between 12 and 14 m s^{-1} in the boundary layer. Comparing the two atmospheric cross sections, the 1200 UTC boundary layer is colder and drier at the western side, but at the eastern side the cross sections have similar θ_e and q values. This suggests there are increased surface sensible and latent fluxes at 1200 UTC, as one may expect given a colder, drier overlying ABL. This is corroborated by a greater depth with fetch of the ABL at the later time; it is 300 m deeper.

In summary, the cold-air outbreak resulted in a dramatic deepening of the marine boundary layer with fetch, and an increase in depth over time. The boundary layer over the Labrador Sea was unstable to moist convection, and satellite imagery from 2127 UTC 7 February (not shown) and 1119 UTC 8 February (Fig. 1) shows that this moist convection was organized into two-dimensional cloud streets. We now examine cross sections of these cloud streets and the hypothesis that

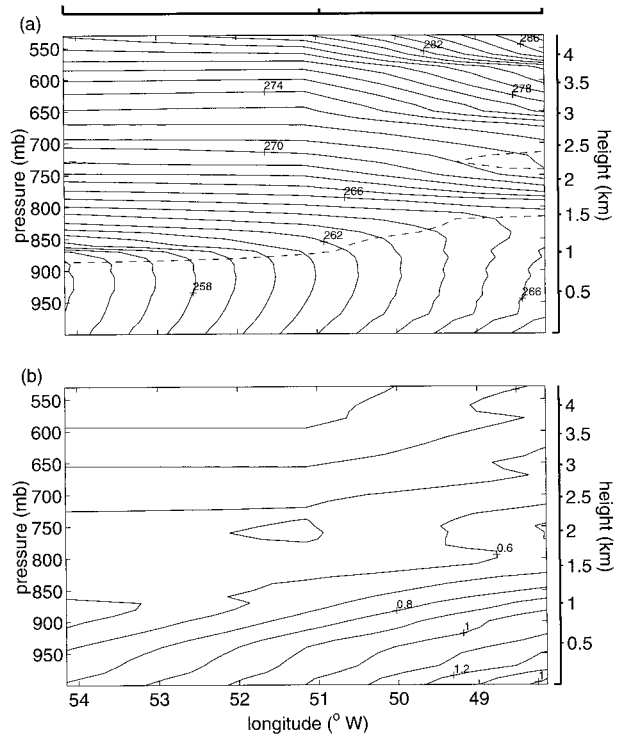


FIG. 6. Cross sections of (a) θ_e and (b) q for the 0200 UTC dropsonde run. The cross-section location and plot details are the same as Fig. 4.

it is horizontal roll vortices that are generating these linear bands.

5. Roll vortices

a. Low-level aircraft data

Figure 7 shows traces of temperature (T , upper lines) and specific humidity (q , lower lines) from the low-level portion of the 1200 UTC 8 February flight. The panels are from the lowest leg (approximately 170 m above sea level) of stacks 1, 2, and 3 as indicated. One can see there is a general warming of the air between successive stacks, with leg-mean temperatures of -23.46° , -21.90° , and -18.76°C , respectively; and a general moistening of the air, with leg-mean specific humidities of 0.45 , 0.49 , and 0.66 g kg^{-1} (Table 1). The temperature trace is dominated by small-amplitude noise, indicative of a turbulent convective ABL (e.g., Garratt 1992). In contrast, there is a well-defined oscillation in the water vapor (i.e., q) signature. This oscillation becomes larger in amplitude through successive stacks and clearly marks out a possible roll vortex signature, with a wavelength of 4–5 km. The peaks of high q one would expect to be collocated with updrafts, moisture being evaporated from the ocean's surface and lifted upward. The troughs of low q one would expect to be collocated with dry downdrafts (e.g., Etling and Brown 1993). This expectation is corroborated by comparing the q traces with

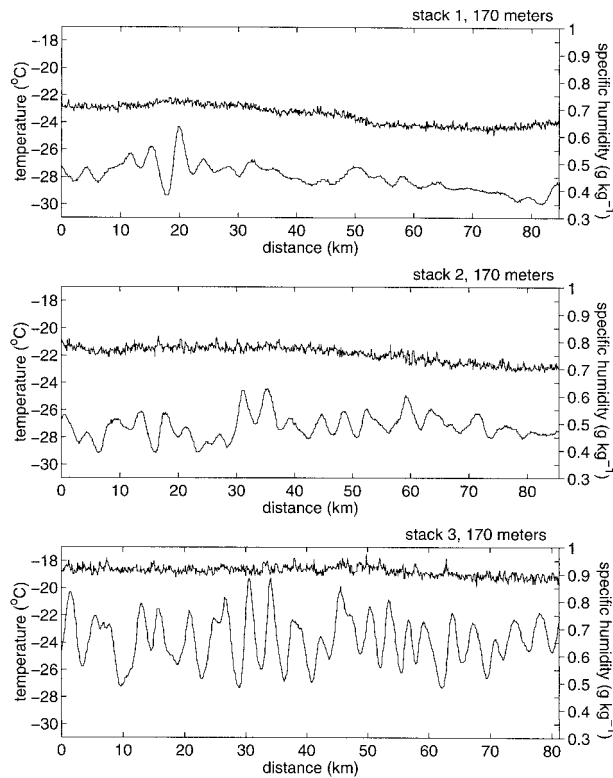


FIG. 7. Traces of temperature (upper curves) and specific humidity (lower curves) for the lowest leg of stacks 1, 2, and 3 as indicated. Data are sampled at 1 Hz from the flight-level sensors. The location of the stacks is shown in Fig. 1. The *x* axis is distance in km from the northern end of each stack. A roll vortex signature is clear from the oscillation in the specific humidity.

the cross section in Fig. 4b. In stack 3 for example, the leg-mean *q* is 0.66 g kg⁻¹ (Table 1) and the maxima and minima are typically 0.8 and 0.5 g kg⁻¹, respectively (Fig. 7). By comparing these values with those in Fig. 4b, one can see the leg-mean *q* value corresponds well with the cross-sectional *q* value at this height (170 m). Similarly a maximum value of 0.8 g kg⁻¹ corresponds to a near-surface *q* value, and a minimum of 0.5 g kg⁻¹

to a level around 1100 m, near the ABL top. This water vapor pattern strongly suggests the boundary layer flow was organized into horizontal roll vortices, which were circulating air between the ocean's surface and the ABL top. The traces shown in Fig. 7 are consistent with cutting through consecutive updrafts and downdrafts in the roll vortices. Note it is interesting that the one large *q* peak in stack 1 (at 20 km) corresponds, given the time lag, with the cloud streamer funneling out of Goose Bay (54°N, 58°W) visible in Fig. 1.

The *T* and *q* traces in the panels shown in Fig. 7 are also representative of the legs at the other heights. Comparing between the three heights (170, 300, and 450 m) at any one stack, there is no apparent correlation with height on the scale of the roll vortex signal. This may be due to changes in roll structure occurring in the time between the aircraft legs, or due to some variability along the roll vortices. By checking dewpoint temperature traces it was found that only a couple of the *q* peaks are fully saturated at the 170-m level. However, there are a few more saturated peaks at the 450-m level, especially in stack 3. This is consistent with the increase in leg-mean relative humidity with height (Table 1), although note the actual water vapor content (e.g., *q* in Table 1) decreases with height, consistent with Fig. 4b. Visual observations were of clear skies at stack 1 and of increasing cloud at stacks 2 and 3, respectively. At stack 3 the 170-m leg was flown below the cloud deck, and there was increasing cloud (decreasing visibility) with height.

The roll vortex signature is also evident in the flight-level pressure or equivalently the radar altimeter data (not shown). This shows a well-defined oscillation that increases in amplitude with fetch, although with more high-frequency noise than the *q* data. Although the aircraft aimed to be flown at legs of constant height, there were unavoidable variations of 10–20 m, which lead to flight-level pressure variations of 1–2 mb. We suggest these variations are caused by the plane being bobbed up and down in the roll updrafts and downdrafts. Figure 8 shows plots of the cross-roll wind, defined as the wind

TABLE 1. Leg means from the low-level aircraft data.

| | Leg height (m) | Leg length (km) | Start time (UTC) | Wind speed (m s ⁻¹) | <i>T</i> (°C) | <i>θ</i> (K) | <i>q</i> (g kg ⁻¹) | RH (%) | Flight level pressure (mb) | Sea level pressure (mb) | <i>ρ</i> (kg m ⁻³) |
|---------|----------------|-----------------|------------------|---------------------------------|---------------|--------------|--------------------------------|--------|----------------------------|-------------------------|--------------------------------|
| Stack 1 | | | | | | | | | | | |
| | 178 | 84.55 | 1358 | 13.233 | -23.46 | 251.132 | 0.4476 | 74.16 | 977.9 | 1000.4 | 1.366 |
| | 317 | 84.54 | 1418 | 12.887 | -24.665 | 251.311 | 0.4377 | 78.95 | 959.2 | 1000.2 | 1.346 |
| | 439 | 84.49 | 1439 | 14.226 | -25.657 | 251.509 | 0.4228 | 81.91 | 943.2 | 1000.2 | 1.329 |
| Stack 2 | | | | | | | | | | | |
| | 156 | 85.21 | 1520 | 14.453 | -21.897 | 252.64 | 0.4892 | 71.16 | 978.9 | 998.2 | 1.358 |
| | 304 | 85.26 | 1539 | 14.481 | -23.294 | 252.712 | 0.4691 | 75.46 | 959 | 997.9 | 1.338 |
| | 464 | 85.23 | 1559 | 14.776 | -24.792 | 252.778 | 0.4574 | 81.97 | 938.2 | 997.4 | 1.317 |
| Stack 3 | | | | | | | | | | | |
| | 182 | 81.11 | 1641 | 13.451 | -18.759 | 256.211 | 0.6593 | 73.05 | 973.4 | 995.8 | 1.334 |
| | 288 | 81.19 | 1700 | 14.148 | -19.82 | 256.196 | 0.6331 | 75.56 | 959.4 | 995.7 | 1.32 |
| | 455 | 81.13 | 1721 | 14.479 | -21.376 | 256.258 | 0.5924 | 78.91 | 938.2 | 995.7 | 1.299 |

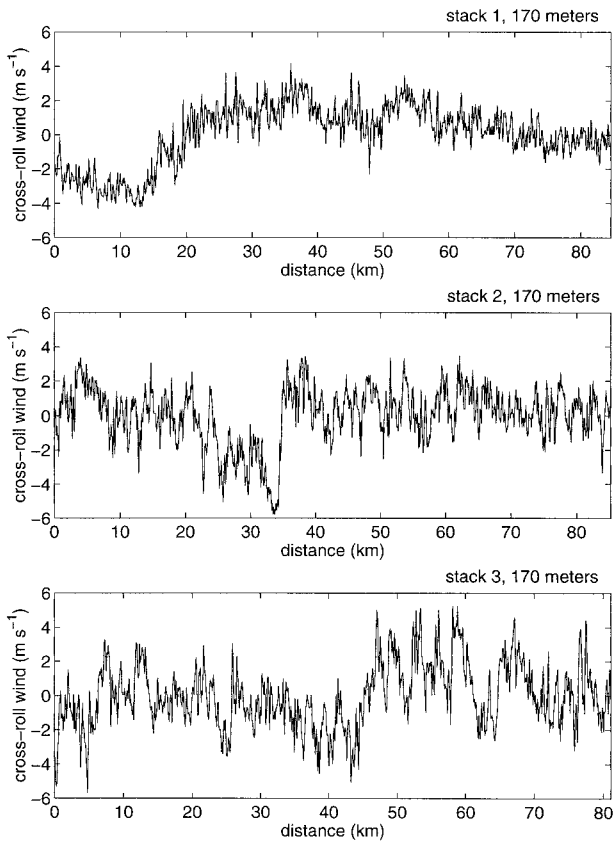


FIG. 8. Cross-roll winds for the lowest leg of stacks 1, 2, and 3, from the flight-level data. Plot details as for Fig. 7.

component perpendicular to the mean wind direction for each leg. The panels are from the lowest leg of stacks 1, 2, and 3, respectively, as for Fig. 7. This is approximately the same wind component as that shown in Fig. 5a, although recall that it was defined as perpendicular to the dropsonde leg direction; the flight-level definition implies that the coordinate system will vary slightly with each leg. There is a considerable amount of high-frequency variability in the cross-roll wind, due to the turbulent nature of the boundary layer flow. There is also some lower-frequency mesoscale structure in the data, which could be reflecting, for example, variations within the synoptic-scale low pressure system, or upstream topographic flow distortions. Note this mesoscale structure is coherent with height in each stack; for example, the strong shift from -3 to $+3$ m s^{-1} at around 45 km in the 170-m leg of stack 3 is echoed in the 300- and 450-m legs of stack 3. Such mesoscale structure is also seen in the alongroll winds, and to a lesser extent the temperature trace, and the water vapor signature. Looking at the raw wind data it is difficult to discern a roll vortex signal comparable to that of q in Fig. 7, as the high-frequency variability camouflages any roll organization.

In short, an examination of the raw flight-level data shows several separate scales in the boundary layer.

There is a high-frequency or “turbulence” scale, illustrated by the temperature or wind traces; a “roll vortex scale,” a well-defined oscillation in water vapor; and a “mesoscale variation” over the low pressure system, for example, the 1°C decrease in temperature with distance south in stack 1 (Fig. 7).

b. Spectral analysis

Spectral analysis techniques have been employed to quantify the dominant scales in the flight-level data. Spectral analyses of all relevant variables were carried out with selected results shown here. For analysis purposes each leg of each stack was treated as a separate data sequence. Power spectra were estimated for the full length of each data sequence, with a Hanning window of the same length used to taper the ends of the sequence. The mean and linear trend were removed from the data. To try to reduce the inevitable sampling problems that result from the relatively short data sequences (typically 900 points), a three-point moving average in the spectral domain was employed. For convenience only a portion of the frequency domain is shown. The frequency domains down to the Nyquist frequency of 1 Hz were examined, but there was no significant power at higher frequencies. The statistical significance of the peaks can be gauged by comparing to the 99% confidence levels for white noise (the dashed line in each panel). It would be expected that only 1% of a white noise spectrum would exceed this level, although recall this is a purely statistical test and the relevance of any significant peaks should be judged on a geophysical basis.

Figure 9 shows normalized power spectra of T and q for the lowest leg of stacks 1, 2, and 3, that is, the traces shown in Fig. 7. There is a consistent and significant peak in the water vapor signal in the 4–5-km range. This has therefore been defined as the primary *roll vortex scale*. There is also power at longer wavelengths, at 7 km in stack 3, and around 15–20 km in all three stacks, although given the legs were approximately 85 km this may not be significant. The consistent peak in q suggests a roll wavelength of 4–5 km in a boundary layer of depth 1–1.2 km, thus a roll aspect ratio of between 3:1 and 5:1. This is typical of aspect ratios that have been observed in other studies (Etling and Brown 1993; Atkinson and Zhang 1996). The power spectra of T show almost no power at this roll vortex wavelength; instead all the power is toward the lower frequencies and is presumably a representation of the mesoscale temperature variation over the low system (Fig. 7).

A coherent roll signature in water vapor with the absence of a roll signature in the temperature is unusual for roll vortex regimes. Previous aircraft observations have always found signatures of the roll vortices in both fields (e.g., Atlas et al. 1986; Chou and Ferguson 1991; Martin and Bakan 1991; Brümmer et al. 1985). Indeed it appears to have been the tacit assumption that the roll

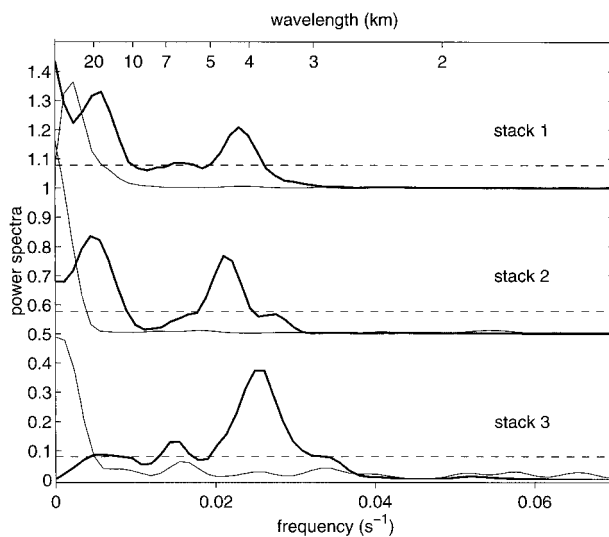


FIG. 9. Normalized power spectra of temperature (thin lines) and specific humidity (thick lines) for the lowest legs of stacks 1, 2, and 3 as indicated. Note for clarity the spectra of stacks 1 and 2 have been offset by 1.0 and 0.5. The dashed horizontal lines give a statistical measure of the significance of the peaks (see text). The peak in specific humidity at 4–5 km has been defined as the roll vortex signature.

temperature signature was an intrinsic part of the roll vortex structure, a result of vertical temperature advection, where warmer air is advected up by the updrafts, and colder air is brought down by downdrafts. In this case, however, the lack of temperature signature implies the vertical temperature advection was small. In addition, we would argue that the extremely low temperatures would have resulted in very small absolute amounts of water vapor in the atmosphere, which means that any latent heat of condensation produced in the roll updrafts would be minute. In other words, the tendency for moisture-rich updrafts to be associated with higher temperatures is considerably reduced. For example, for the lowest leg ($170 \text{ m} \approx 0.16z_i$) air temperatures were typically -20°C (Table 1), a temperature that would allow only 0.8 g kg^{-1} of water vapor at saturation. In contrast, in the cases noted above, air temperatures at this height were, respectively, -5° , -5° , 13° , and 15°C , allowing 2.7 , 2.7 , 9.5 , and 10.8 g kg^{-1} of water vapor, respectively, up to an order of magnitude more water vapor. To give an idea of the amount of latent heat this can *potentially* generate, it is useful to imagine an air parcel in the ABL being lifted, due to moist convection, from the surface to say 900 mb. If equivalent potential temperature (θ_e) is conserved, then at temperatures of -20°C this leads to an increase in potential temperature $\Delta\theta \approx 0.5^\circ\text{C}$. At temperatures around -5°C then $\Delta\theta \approx 2^\circ\text{C}$, and at 15°C then $\Delta\theta \approx 4.5^\circ\text{C}$. This suggests the role of latent heat production due to condensation in roll updrafts will vary tremendously with ambient temperature. In this case it can only be relatively small, which partly explains the lack of roll vortex temperature

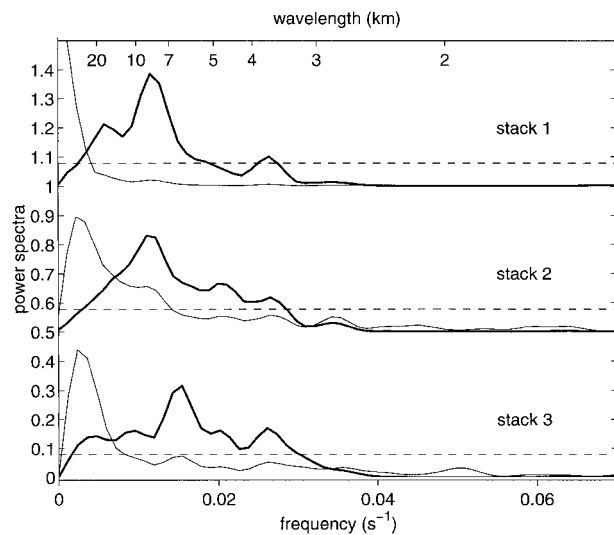


FIG. 10. Normalized power spectra of cross-roll wind (thin lines) and cross-roll convergence (thick lines) for the lowest legs of stacks 1, 2, and 3 as indicated; details as in Fig. 9.

signal. However, in warmer regimes it is certain to be partly responsible for any roll vortex temperature signal. To our knowledge, the contributions of these two processes have not been examined in previous studies.

Figure 10 shows power spectra of the cross-roll wind (i.e., Fig. 8) and the cross-roll convergence. There is power at longer wavelengths in the spectra of the cross-roll wind, possibly representing the mesoscale variation across the legs, but there are only a number of small peaks between 3 and 10 km in stacks 2 and 3. There are significant peaks in the cross-roll convergence at all three stacks at around 3–5 km and around 7–10 km. One can view the cross-roll convergence as a proxy for vertical velocity, so these peaks suggest a pattern of roll updrafts and downdrafts on scales of both 3–5 and 7–10 km. It is difficult to discern such variability in the raw cross-roll convergence traces, due to the large high-frequency variability that is present. However, this match between the water vapor peaks and the convergence peaks is positive evidence for a horizontal roll vortex regime causing the cloud streets seen in Fig. 1. Further scale and phasing relationships have been examined via cospectral analyses. For example, cospectral analyses for q and cross-roll convergence appear similar to the q lines in Fig. 9. Unfortunately the phase relationships are too noisy to obtain meaningful results.

To summarize, spectral analysis of the flight-level data indicates a roll vortex scale of 4–5 km, with this signal particularly clear in the water vapor data and as one moves downstream. Unusually the roll vortex scale is not represented in the temperature spectra. We suggest that this lack of a roll temperature signal is due to small vertical temperature advection, combined with low ambient temperatures limiting the amount of latent heating due to condensation that can occur in the updraft re-

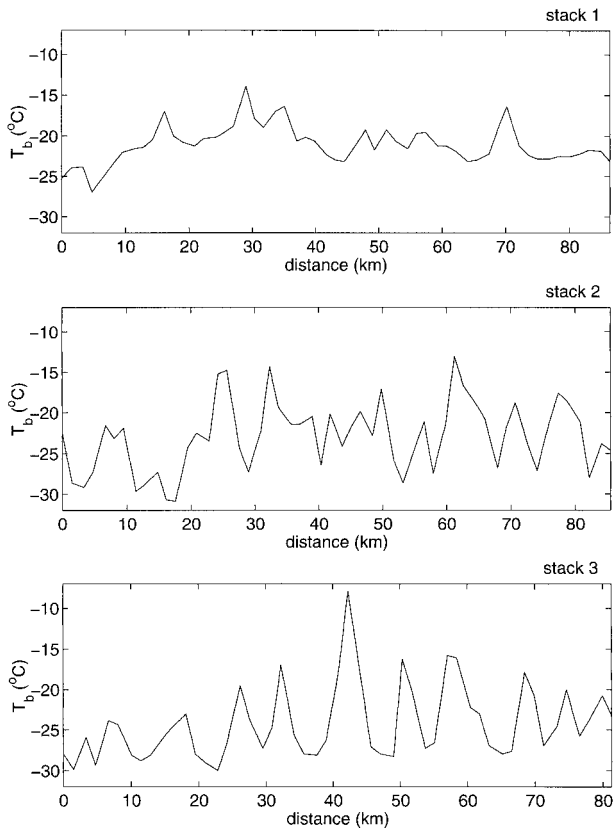


FIG. 11. Brightness temperature T_b for stacks 1, 2, and 3, extracted from the AVHRR 1119 UTC satellite data (Fig. 1). The traces shown here are for channel 4 ($10.8 \mu\text{m}$) T_b .

gions. There is also power on longer wavelengths, thought to be due to mesoscale variations over the flight legs, and on a 7–10-km scale in the cross-roll convergence spectra.

c. Satellite imagery

Figure 11 shows cross sections of Advanced Very High Resolution Radiometer (AVHRR) channel 4 ($10.8 \mu\text{m}$) brightness temperature (T_b) extracted along the stack lines of the 1119 UTC satellite image shown in Fig. 1. This was the closest satellite pass available to the time of the aircraft flights (1200–1700 UTC). There is an oscillation in T_b between the cold cloud tops and the relatively warm emissions from between the clouds. Note that the cloud-top T_b 's are similar to the dropsonde temperatures at the boundary layer top, indicating the cloud tops and the temperature inversion are at the same height. The oscillation in T_b becomes clearer and more regular with downstream distance. Comparing the T_b traces with the flight-level q traces, it is clear that the cloud street scale and the roll vortex scale are different. Indeed a visual assessment suggests that the primary cloud street wavelength is roughly double the primary q wavelength.

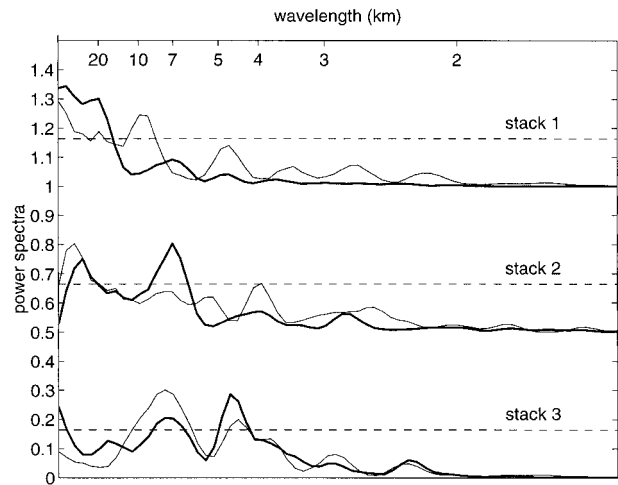


FIG. 12. Normalized power spectra of T_b channel 3 (thin lines) and channel 4 (thick lines) for the 1119 UTC AVHRR data, stacks 1, 2, and 3 as indicated. The spectra of stacks 1 and 2 have been offset by 1.0 and 0.5 as same as in Figs. 9 and 10. A measure of the statistical significance of the signal is shown as a dashed horizontal line. The peak at 7–10 km in stacks 2 and 3 has been defined as the cloud street scale.

To quantify the cloud street scale, a spectral analysis of T_b data sequences was carried out. The AVHRR images have a pixel size of 1.1 km at nadir, so looking at 85-km length legs provides only a very short sequence of data. To reduce the associated sampling problems, the data sequences were extended on either side of the aircraft stacks, at the same orientation, to roughly twice their original length. This was long enough to produce a more reliable data sequence without excessive mesoscale variation in the cloud patterns (Fig. 1). Note that the original T_b data sequences (Fig. 11) were also examined, and the extension procedure did not bias the location of the main spectral peaks. The data sequences cross the image pixels at an angle, so the values represent irregular distance segments. An interpolation of the data onto a regular distance grid is therefore required and a 1-km grid was chosen. The power spectra were then estimated following the same procedure as for the flight-level data, including a three-point moving average in the spectral domain. Figure 12 shows power spectra of T_b for both channel 3 ($3.7 \mu\text{m}$) and channel 4. In all the stacks there is a statistically significant peak at 7–10 km, which is therefore defined as the *cloud street scale*. There is also power at longer wavelengths reflecting the mesoscale changes in cloud cover and at shorter wavelengths where there is a peak at 4–5 km echoing the primary roll vortex wavelength seen in the water vapor spectral analysis. The 7–10-km peak corresponds well with the peak seen in the cross-roll convergence spectra.

d. Multiscale roll vortices

Spectral analysis has aided in the categorization of two scales in the roll vortex regime: a roll vortex scale

of 4–5 km most clearly defined in the aircraft water vapor records, and a cloud street scale of 7–10 km—the dominant scale in the satellite-derived brightness temperatures and also clear in the cross-roll convergence spectra. Separate scales in the same roll vortex regimes have also been observed by Walter and Overland (1980), Atlas et al. (1986), and Hein and Brown (1988). In Walter and Overland's study fog over mainly ice-covered ocean was used to delineate ABL rolls. A hierarchy of scales was suggested from satellite and aircraft data: a (possible) 30-km scale, a 12–15-km scale induced by upstream topography, a 5–6-km scale, and a 1.3–1.7-km scale; the latter two scales both evident in their aircraft data. They suggest the 5–6-km scale may be "due to an irregularity in the roll strength," and the 1.3–1.7-km scale may have been due to an inflection instability of the ABL flow (Brown 1970, 1972). The 1.3–1.7- and 5–6-km scales may be analogous to the roll vortex and cloud street scales seen here. The aspect ratios are similar, given the low inversion height of 660 m in the Walter and Overland study. Hein and Brown (1988) provide evidence for coherent structures at wavelengths centered around 1.2, 2.3, and 5.8 km, which they attribute to, respectively, 3D convection, 2D inflection instability rolls, and an "unknown process." Again z_i is only around 700 m, so the latter two processes have aspect ratios that are similar to our case. They speculate that the longer 6-km signature could be a scale set by convection (rather than horizontal dynamics) or through the augmentation or suppression of shorter-scale rolls. Lidar and aircraft observations were examined in Atlas et al. (1986), who discovered updrafts of aerosol-rich air had been organized into roll vortices, despite an absence of cloud streets. There was a multiscale roll signature in the spectral analysis of their aircraft data, and they conclude that this was due to the enhancement of *some* of the counterclockwise roll cells by a cooperative shear of the cross-roll wind. Note that if a cross-roll shear were to act impartially on a uniform set of roll vortices it would not lead to two concurrent wavelengths (a wavelength being measured from updraft to updraft), but simply a broadening and suppression of neighboring helical rolls, as seen in Kristovich (1993). However, if the shear acts in an irregular manner, to enhance only some cooperative rolls, as suggested by Atlas et al. (1986, their Fig. 12), then two distinct wavelengths would be detected.

The enhancement of some rolls at the expense of others is also seen in the nonlinear two-dimensional numerical model simulations of Sykes et al. (1988). They carried out a number of simulations of roll development within a mean flow, with convection stimulated by a positive surface heat flux. A 4-km roll vortex regime develops initially, but the cloud streets above the roll updrafts then merge together, leading to a larger cloud street wavelength than roll wavelength. This cloud merger is attributed to "wind shear near the inversion." The cloud scale is maintained through the entrainment

of warm air into the ABL, which discourages convection. In the stronger updrafts, latent heat release in the clouds acts as a positive feedback mechanism, enhancing these rolls at the expense of others.

A theoretical platform for the development of multiscale roll vortices is set out by Mourad and Brown (1990). They develop a nonlinear model that allows wave–wave interactions to superpose different scales of roll vortices. Their wave–wave "triad II" produces rolls of 1–4 and 4–10 km simultaneously, in agreement with the two scales of rolls we observed. However, their work does not pinpoint the sources of the interacting waves, for which they offer the possibilities of an inflection instability (Brown 1970, 1972), a mesoscale entrainment instability (Fielder 1984), internal gravity waves (Clark et al. 1986), or some topographic forcing. Note convection is not included in the Mourad and Brown theory, leaving a serious question mark in comparing our case with that theory. In some sense the theory of Mourad and Brown also encompasses the more physical idea of a cross-roll shear enhancing and suppressing certain rolls, as this shear may well be the result of a triad wave member.

With the limitations of the data available we are unable to determine positively the mechanisms that are setting the two scales, the cloud street scale and vortex roll scale, that are evident in our study. The idea of cross-roll shear enhancement of certain rolls at the expense of others could explain the two scales. There is a substantial negative cross-roll shear due to the jet near the inversion height, between stacks 2 and 3 (Fig. 5a), and also in the plane descent at 54°W (not shown). This would imply a strengthening of anticlockwise roll vortices, that is, those with a cooperative shear, at the inversion height. Whether this occurred is unfortunately not known, as the aircraft legs were flown well below this level. If the strengthening occurred in an uneven manner (Atlas et al. 1986; Sykes et al. 1988), perhaps reinforced by latent heat release due to condensation in the stronger updrafts (the 7–10-km peaks in the convergence spectra), then the two separate roll vortex and cloud street scales may have resulted. Alternatively Clark et al. (1986) suggest that a resonant interaction between ABL convection and internal gravity waves can modify the spacing of the convection. It may be possible that such an interaction was going on, and our data are from a stage where both scales were present. There is some evidence that internal gravity waves were forced by the growing ABL (Fig. 4a). There are other possibilities, but given the data at hand, a modification by cross-roll shear, perhaps reinforced by latent heating in the stronger updrafts, seems the most plausible explanation.

6. Surface flux estimates

a. Lagrangian parcel estimates

The low-level portion of the 1200 UTC aircraft flight was planned to be approximately Lagrangian, in the

TABLE 2. Stack differences from flight-level data and the adjusted Lagrangian estimates of surface heat fluxes.

| Stack differences | δt (s) | $\delta\theta$ (K) | δq (g kg ⁻¹) | Column ρ (kg m ⁻³) | H (m) | Sensible fluxes (W m ⁻²) | Latent fluxes (W m ⁻²) |
|-------------------|----------------|--------------------|----------------------------------|-------------------------------------|------------|--------------------------------------|------------------------------------|
| 2-1 | 7402 | 1.393 | 0.038 | 1.2 | 965 ± 100 | 175 ± 35 | 18 ± 4 |
| 3-2 | 7301 | 3.506 | 0.156 | 1.2 | 1028 ± 100 | 476 ± 95 | 79 ± 16 |

sense that a hypothetical “air parcel” was to be regularly sampled as it was advected from over the sea ice to over the open water. Changes in the heat and moisture content of the air parcel could then be attributed to sources or sinks, assuming the horizontal advection terms to be zero. The flight had been planned such that the same air parcels were to be sampled for each leg of each stack, that is, allowing a comparison of leg 1, stack 1 with leg 1, stack 2, and so on (Fig. 3). However, the wind speeds were lower than forecast (by around 5 m s⁻¹) meaning a comparison of legs was not justified. Instead each *stack* position has been treated as a single air parcel extending from the sea surface to the top of the ABL. This idealization is discussed by Bretherton and Pincus (1995). Values of θ and q are assigned to each stack position by averaging together all three legs of that stack. This is justified for θ as the ABL is well mixed (Fig. 4a, Table 1). However, it is less justified for q as the water vapor decreases with height through the ABL (Fig. 4b, Table 1). The measured wind speed and wind direction have been used to calculate the time (δt) for an air parcel to travel between each pair of stacks. The changes in heat ($\delta\theta$) and moisture (δq) over this time δt are then calculated for each pair of stacks. The results are summarized in Table 2.

The increases in potential temperature and water vapor can be attributed primarily to the surface sensible and latent heat fluxes between the ocean and the atmosphere. The warming of the air parcel is largely due to the surface sensible heat flux (SHFX), the moistening is largely due to the surface moisture flux, that is, evaporation from the ocean, leading to a latent cooling of the surface ocean (LHFX). The surface fluxes can therefore be estimated from the following equations:

$$\text{SHFX} + \varepsilon_1 = c_p \rho \frac{\delta\theta}{\delta t} H \quad (1)$$

$$\text{LHFX} + \varepsilon_2 = L \rho \frac{\delta q}{\delta t} H, \quad (2)$$

where c_p is the specific heat capacity of air, ρ is the average density of the column, L is the latent heat of vaporization, H is the height of the air parcel, and the ε_i 's represent residual processes that are discussed below. In this case H is taken as the height of the boundary layer; that is, H is equal to the inversion height z_i (Fig. 4a). If we assume a uniform heating and moistening of the whole air column, consistent with the above assumption of a well-mixed air parcel of height H , then this implies a linear decrease with height of both heat

and moisture fluxes (Garratt 1992). This is consistent with typical turbulent flux profiles in observational studies (Grossman and Betts 1990; Chou and Ferguson 1991). Neglecting the residual terms this gives raw sensible flux estimates of 219 and 595 W m⁻² and raw latent flux estimates of 15 and 66 W m⁻² for stack differences 1-2 and 2-3, respectively.

The above equations are from a simplification of the heat and moisture budget equations as described in Brümmner (1997) or Chang and Braham (1991), for example. There are a number of physical processes that would contribute to these budgets, which we are unfortunately not able to determine from the data. These uncertainties are represented by the terms ε_1 and ε_2 in Eqs. (1) and (2). The physical processes they represent include the following.

- Evaporation of sea spray thrown up from breaking waves. The occurrence of wave breaking, or whitecaps, is a function of wind speed. Wave breaking would be expected to cover $\sim 0.1\%$ of the surface ocean for a 10 m s⁻¹ winds (Garratt 1992), and indeed whitecaps were observed during the flight. This process has the effect of cooling and moistening the air while approximately conserving θ_e . It does not affect the total surface fluxes as it reduces the sensible flux estimate and boosts the latent flux estimate by the same amount. It is thought that the evaporation of sea spray would have been small in this case, as the extremely cold air cannot contain much water vapor, and the relative humidities are high (over 70%). In a somewhat similar cold air outbreak Grossman and Betts (1990) found this term, as a residual, to be less than 10% of their latent heat flux estimate. In the case investigated here the ABL was 10°C colder, thus reducing the rate of evaporation, so for the purposes of a first-order surface flux estimate we assume this term is negligible.
- Condensation of water vapor in the updrafts of the roll vortices. This was occurring as evidenced by the fog streets (see Renfrew et al. 1999) and cloud streets (Fig. 1), and would have the effect of heating and drying the air column. This would imply an overestimate of the sensible heat flux and an underestimate of the latent heat flux by Eqs. (1) and (2). However, in this case, there is no roll signature in the flight-level temperature data (Figs. 7, 9), which suggests the latent heating must have been negligible at the levels flown. Note it would undoubtedly have been larger and higher in the ABL; indeed as discussed in section

5, it may be partially responsible for maintaining the longer cloud street wavelength. Grossman and Betts (1990) account for this contribution as part of their residual terms, which are approximately 20% of the total heat budget and 100% of the total moisture budget. Chang and Braham (1991) also include this process in their residual terms, which are 12% for the heat budget and 6% for the moisture budget (averaged over fetch). In Brümmer (1997) the condensational heating varied from case to case, but was typically 10%–20% of the heat budget and 10%–80% of the moisture budget. In this case, given the very cold ABL and therefore the relatively small amounts of absolute water vapor available for condensation (section 5), it was thought that this process would be toward the lower limit of that seen in other studies. Hence we assume an overestimate of the surface sensible fluxes of 10% (22 and 59 W m^{-2}) and an underestimate of the surface latent fluxes of 10% (1.5 and 6.6 W m^{-2}).

- Turbulent entrainment of heat and moisture across the top of the boundary layer. Typically in a growing convective boundary layer, such as that implied by Figs. 4 and 6, entrainment causes a warming and drying toward the top of the ABL (Garratt 1992). This would imply that our assumption of an air parcel of height H would result in an overestimate of the surface sensible fluxes and an underestimate of the surface latent fluxes. In Grossman and Betts (1990) the turbulent sensible and latent fluxes at the inversion level were $-18 \pm 14\%$ and $-6 \pm 6\%$, respectively, of the turbulent fluxes at the surface. In Chang and Braham (1991) the entrainment of heat was about -10% of the surface heat flux (averaged over the fetch). The entrainment of moisture was about 25% of the average surface moisture flux. In Brümmer (1997) the entrainment heat flux varied considerably from case to case, from -10% to $+80\%$, and the entrainment of moisture was regarded as negligible. Given what is regarded as typical, in conjunction with the studies noted above, it was decided to assume entrainment heat and moisture fluxes modifying the raw estimates by $-10 \pm 10\%$ and $+10 \pm 10\%$, respectively.
- Mean vertical inflow/outflow of heat and moisture across top of the air column. This is not known, but is typically much smaller than ABL top entrainment and is assumed to be negligible for this calculation.
- Radiative flux convergence into the column. This is difficult to determine as the radiative flux through the top of the air parcel is unknown. In Brümmer (1997) it is assumed zero in most cases, and we assume the same here.

A final source of uncertainty on these estimates is the height of the boundary layer H , determined from the dropsonde data (Fig. 4a). The dropsonde data retain features on the scale of around 10 mb in the vertical, suggesting an error δH of ± 100 m. With H equal to 965

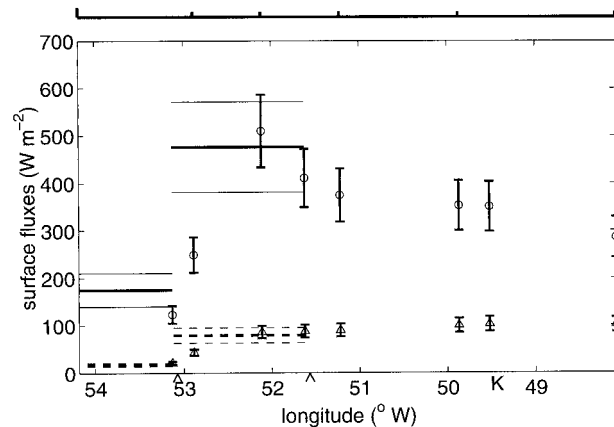


FIG. 13. Surface sensible and latent heat flux estimates at 1200–1800 UTC for a cross section of the cold air outbreak. The horizontal lines show the estimated sensible (solid) and latent (dashed) heat fluxes from the Lagrangian parcel method, Eqs. (1) and (2), for stack differences 1–2 (54.2° – 53.1° W) and 2–3 (53.1° – 51.6° W). Bulk flux estimates from Eqs. (3) and (4) are marked by circles for the sensible fluxes, and the triangles for the latent fluxes. The data for the bulk fluxes are a mix of flight-level means, dropsonde data, and Knorr data; see text for details.

and 1028 m (Table 2), this implies a further uncertainty of approximately $\pm 10\%$ on the flux estimates.

As outlined above there are significant uncertainties in the surface flux estimates. However, such uncertainties plague all maxine ABL studies and lead to residuals in any budget calculations, for example, Grossman and Betts (1990), Chang and Braham (1991), and Brümmer (1997). This is the first low-level aircraft dataset obtained over the Labrador Sea, an area of ongoing research in oceanic deep convection. Hence we feel a first-order estimate of surface heat fluxes is warranted, despite these uncertainties. Thus the raw sensible heat fluxes are reduced by $20 \pm 20\%$ to give adjusted estimates of 175 ± 35 and 476 ± 95 W m^{-2} for stacks 1–2 and 2–3, respectively, and the raw latent heat fluxes are boosted by $20 \pm 20\%$ to give adjusted estimates of 18 ± 4 and 79 ± 16 W m^{-2} . These Lagrangian surface flux estimates are plotted as horizontal lines in Fig. 13.

b. Bulk flux estimates

It is interesting to compare the above Lagrangian surface flux estimates with those obtained via the bulk coefficient method (e.g., Garratt 1992):

$$\text{SHFX} = C_{\theta} V_a (\theta_s - \theta_a) \rho c_p \quad (3)$$

$$\text{LHFX} = C_q V_a (q_s - q_a) \rho L, \quad (4)$$

where C_{θ} and C_q are the bulk coefficients, V_a is the mean wind speed, θ_s the sea surface potential temperature, θ_a the potential temperature of the air, q_s is the saturated specific humidity for the sea surface temperature [$q_s = q_{\text{sat}}(T_s)$], and q_a is the specific humidity of the air. The bulk coefficients are taken as constant values

of $C_\theta = 1.24 \times 10^{-3}$ and $C_q = 1.56 \times 10^{-3}$, with error bars of $\pm 15\%$. The values of the coefficients are taken from the parcel budget study of Grossman and Betts (1990), as their observed conditions were close to those of this case. They also investigated an extreme cold air outbreak with a boundary layer unstable to moist convection, observations of fog and whitecaps, and with fetch and low-level wind speeds similar to our case. The coefficients used are within the range suggested by reviews of this method, for example, Garratt (1992). The error bars of $\pm 15\%$ are also suggested by the discussion in Garratt. Note the larger value for the latent heat coefficient is backed theoretically (Garratt 1992) and is also consistent with the review paper of Smith (1988).

The data used are from averages of the lowest leg of the aircraft stacks (Table 1), from the dropsondes, and from the R/V *Knorr*. The sea surface temperatures were linearly interpolated between -1.5°C at the ice edge (taken as 54°W , halfway between stacks 1 and 2) and 3.25°C measured at the *Knorr* (see Figs. 1 and 13 for location). The temperature assumed at the ice edge is a typical melting/freezing temperature for seawater. The *Knorr* SST is the average "bucket temperature" from 1200 to 1730 UTC 8 February. The wind data from the dropsondes were not used, as it was felt these instantaneous "point" measurements may not be representative of mean values. The lowest-level dropsonde winds ranged between 10.8 and 16.9 m s^{-1} for heights of between 400 and 500 m above sea level. Instead, the nearest time-averaged wind speed to each location was used, that is, V_a 's of 14.45 and 13.45 m s^{-1} for the lowest legs of stacks 2 and 3, respectively (Table 1), and 13.66 m s^{-1} for the 10-m *Knorr* wind speed averaged from 1200 to 1730 UTC. The time-averaged wind speeds are relatively close to each other and close to the middle of the range of the dropsonde wind data. The V_a data were not corrected for height. The relative humidities from the dropsondes were not used either. Some of the sondes fell through the boundary layer cloud streets and had relative humidities of 100%, whereas others fell through the clear downdrafts between the cloud streets and had relative humidities of 70%–90%. To avoid this sampling inconsistency all relative humidities were taken as 70%. This was chosen as a representative figure, given the lowest-level aircraft leg averages (71% and 73%; Table 1) and a *Knorr* relative humidity of 69% from 1200 to 1730 UTC. This approach gives an "average picture" of the bulk latent fluxes. Clearly the inhomogeneous roll vortex regime would have a significant impact on the spatial distribution of the latent fluxes, with an enhanced moisture flux under the updrafts, and a reduced moisture flux under the downdrafts. Finally the bulk fluxes were weighted by the sea ice concentration (e.g., Fig. 1). The westernmost two values were multiplied by 0.25 and 0.5, respectively, that is, making the simple assumption that, for example, 75% ice concentration would reduce the surface fluxes by 75%. The bulk flux estimates were calculated as detailed

above and are plotted in Fig. 13. There is a good match between the bulk and Lagrangian estimates for both the sensible heat fluxes and the latent heat fluxes.

c. A comparison of two soundings

Two aircraft missions were flown into the cold-air outbreak along the same dropsonde leg 10 h apart (Figs. 4 and 6). It was realized that a comparison between the most westerly sounding from the early flight (0340 UTC 8 February) and the most easterly sounding from the later flight (1230 UTC) was approximately Lagrangian. In other words, an air parcel in the mixed ABL advected at 12 m s^{-1} would travel the approximate distance between the release points of the two sondes over 9 h. This wind speed is consistent with that measured (Fig. 5, Table 1). So it is therefore possible to compare the two soundings and estimate the integrated surface fluxes from the heat and moisture changes in the boundary layer. Figure 14a plots potential temperature and Fig. 14b specific humidity for the early sondes (thick lines) and later sondes (thin lines). A substantial warming, moistening, and deepening of the ABL is seen over this time. The potential temperatures in the free troposphere remain similar, while there is a small drying of the free troposphere. The similar θ values in the free troposphere indicate our Lagrangian parcel assumption is reasonable.

Over the 9-h period the boundary layer height is lifted from approximately 1100 to 1800 m. Integrating between the curves in Fig. 14 (over the height of the ABL) gives raw estimates of the surface fluxes, which have then been adjusted in the same manner as the Lagrangian surface flux estimates in section 6a. The average surface sensible heat flux is $429 \pm 86 \text{ W m}^{-2}$ over the 9 h. The gain in moisture in the boundary layer suggests an average surface latent heat flux of $79 \pm 16 \text{ W m}^{-2}$.

d. Discussion

Three indirect estimates of the surface sensible and latent heat fluxes have been made that are broadly consistent with one another. Between 1200 and 1800 UTC the surface sensible fluxes were approximately $500 \pm 100 \text{ W m}^{-2}$ off the ice edge, and decreasing with downstream distance; and the surface latent fluxes were approximately $100 \pm 20 \text{ W m}^{-2}$ over the length of the cross section (Fig. 13). We should note some reservations in the Lagrangian latent heat flux estimate, as the ABL was not well mixed in terms of water vapor, as we have assumed in section 6a. The unaccounted for vertical gradient of q would imply that the surface latent fluxes may be underestimated. The Bowen ratio, defined as $B = \text{SHFX}/\text{LHFX}$, varied from about 5 to 3, decreasing with fetch. These relatively high values of B (e.g., Garratt 1992) are no doubt due to the extremely cold air restricting the amount of evaporation.

This snapshot picture is supported by an integrated

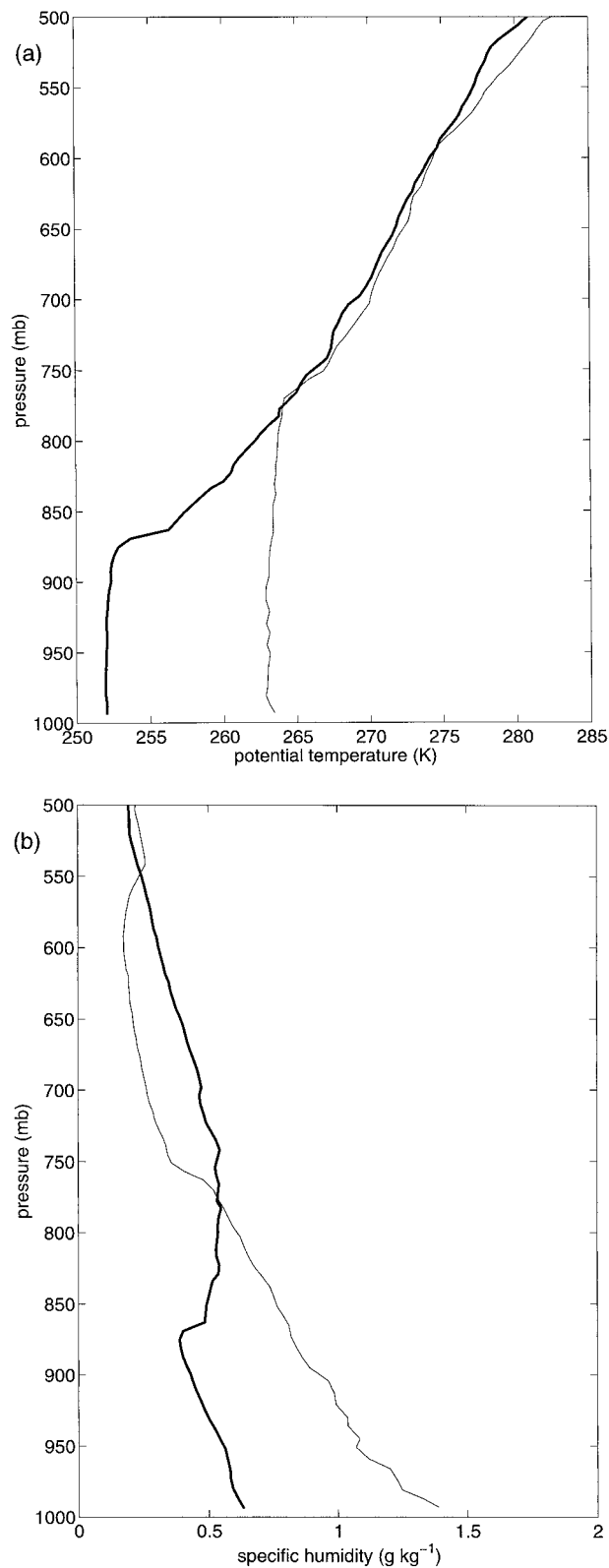


FIG. 14. A comparison of (a) potential temperature and (b) specific humidity from two soundings. The sondes were released at 0340 UTC (thick lines) and 1230 UTC (thin lines) at the far western and eastern ends, respectively, of the dropsonde cross section (see Figs. 1, 4, 6).

estimate, an average over the previous 9-h period. The adjusted integrated sensible and latent fluxes were 429 and 79 W m^{-2} , respectively. These estimates are consistent with the spatial distribution of fluxes shown in Fig. 13. They are also consistent with an increase in surface fluxes between 0200 and 1200 UTC (Figs. 6 and 4). A comparison of the surface fluxes at these two times can be obtained by comparing the heights of the boundary layer. Simple theory (e.g., Garratt 1992) suggests a convectively growing boundary layer has an inversion height $z_i = Cx$, where x is downstream distance and C is a constant proportional to surface heat flux, upstream stratification, and entrainment. From Figs. 6 and 4 one can obtain estimates of C by comparing z_i and x . Assuming the upstream stratification and entrainment remain constant, these suggest the surface sensible heat flux at 1200 UTC is roughly twice that at 0200 UTC, qualitatively consistent with the estimated surface sensible fluxes.

7. Conclusions

Observations of an extreme cold-air outbreak over the Labrador Sea have been presented and analyzed. Cold dry boundary layer air was observed to stream off the continent over the relatively warm ocean, where it rapidly warmed and moistened in a regime of shallow roll convection. Two cross sections through the cold air, 10 h apart, illustrate a dramatic deepening of the boundary layer over this time. The boundary layer height slopes from 850 to 1500 m (over 380 km from west to east) at 0200 UTC, and from 850 to 1800 m 10 h later. This growth of the boundary layer, and the increased warming and moistening with fetch seen in the 1200 UTC cross section, indicate an increase in the surface sensible and latent heat fluxes over this period.

Low-level aircraft measurements combined with AVHRR satellite imagery have been used to describe the roll vortex regime. The aircraft data show horizontal rolls of wavelength 4–5 km (aspect ratio between 3:1 and 5:1). This roll vortex scale is clear in the water vapor and cross-roll convergence spectra, but unusually is *not* evident in the temperature data. This absence is thought to be due to a lack of vertical temperature advection, combined with only the minute amounts of latent heating due to condensation that were possible, in this extremely cold boundary layer. Spectral analysis of contemporaneous satellite imagery shows a dominant cloud street scale of 7–10 km, as well as a signal at the roll vortex scale. The 7–10 km signal is also clear in the cross-roll convergence spectra. This multiscale regime may be explained by the enhancement of some

←

The comparison is approximately Lagrangian for an ABL air parcel, so the significant heating and moistening in the ABL must be due to sources and sinks.

roll vortices at the expense of others by a cross-roll shear of the boundary layer wind, reinforced by latent heating in the stronger updrafts.

Surface flux estimates have been made using three indirect methods: a Lagrangian estimate made by approximately following an air parcel with the aircraft; a bulk flux estimate utilizing aircraft, dropsonde, and ship data; and an integrated estimate made by comparing two soundings. The three indirect estimates are consistent and suggest surface sensible fluxes of approximately 500 W m^{-2} and surface latent fluxes of approximately 100 W m^{-2} off the ice edge, with uncertainties of $\pm 20\%$ on these values (Fig. 13).

Acknowledgments. The Labrador Sea Deep Convection Experiment is supported by the Office of Naval Research. We would like to thank all in the 53d Squadron of the USAF Hurricane Hunters, and the St. John's Weather Centre, as well as Marco De La Cruz, John Mavriyannakis, Mariusz Pagowski, Vladimir Smirnov, and Sudharshan Sathiyamoorthy at the University of Toronto for their support during the field program. Simon Chang and Teddy Holt at the Naval Research Laboratory, Monterey, provided the COAMPS real-time forecasting data. The one day of state variable data from the R/V *Knorr* used in the bulk flux calculations is courtesy of Peter Guest. We would also like to thank Keith Alverson, Dick Bailey, Peter Guest, Mariusz Pagowski, Mike Pedder, and John Talbot for useful discussions on aspects of this work.

REFERENCES

- Alpers, W., and B. Brümmer, 1994: Atmospheric boundary layer rolls observed by the synthetic aperture radar aboard the ERS-1 satellite. *J. Geophys. Res.*, **99**, 12 613–12 621.
- Asai, T., 1970: Stability of a plane parallel flow with variable vertical shear and unstable stratification. *J. Meteor. Soc. Japan*, **48**, 129–139.
- Atkinson, B. W., and J. W. Zhang, 1996: Mesoscale shallow convection in the atmosphere. *Rev. Geophys.*, **34**, 403–431.
- Atlas, D., B. Walter, S.-H. Chou, and P. J. Sheu, 1986: The structure of the unstable marine boundary layer viewed by lidar and aircraft observations. *J. Atmos. Sci.*, **43**, 1301–1318.
- Bretherton, C. S., and R. Pincus, 1995: Cloudiness and marine boundary layer dynamics in the ASTEX Lagrangian experiments. Part I: Synoptic setting and vertical structure. *J. Atmos. Sci.*, **52**, 2707–2723.
- Brown, R. A., 1970: A secondary flow model for the planetary boundary layer. *J. Atmos. Sci.*, **27**, 742–757.
- , 1972: On the inflection point instability of a stratified Ekman boundary layer. *J. Atmos. Sci.*, **29**, 850–859.
- Brümmer, B., 1997: Boundary layer mass, water and heat budgets in wintertime cold-air outbreaks from the arctic sea ice. *Mon. Wea. Rev.*, **125**, 1824–1837.
- , S. Bakan, and H. Hinzpeter, 1985: KONTUR: Observations of cloud streets and open cellular structures. *Dyn. Atmos. Oceans*, **9**, 281–296.
- Chang, S. S., and R. R. Braham, 1991: Observational study of a convective internal boundary layer over Lake Michigan. *J. Atmos. Sci.*, **48**, 2265–2279.
- Chou, S.-H., and M. P. Ferguson, 1991: Heat fluxes and roll circulations over the western Gulf Stream during an intense cold-air outbreak. *Bound.-Layer Meteor.*, **55**, 255–281.
- Clark, T. L., T. Hauf, and J. P. Kuettner, 1986: Convectively forced internal gravity waves: Results from two-dimensional experiments. *Quart. J. Roy. Meteor. Soc.*, **112**, 899–926.
- Etlings, D., and R. A. Brown, 1993: Roll vortices in the planetary boundary layer: A review. *Bound.-Layer Meteor.*, **65**, 215–248.
- Faller, A. J., and R. E. Kaylor, 1966: A numerical study of instability of the laminar Ekman boundary layer. *J. Atmos. Sci.*, **23**, 466–480.
- Fielder, B. H., 1984: The mesoscale stability of entrainment into cloud-topped mixing layers. *J. Atmos. Sci.*, **41**, 92–101.
- Garratt, J. R., 1992: *The Atmospheric Boundary Layer*. Cambridge University Press, 316 pp.
- Grossman, R. L., and A. K. Betts, 1990: Air–sea interaction during an extreme cold air outbreak from the eastern coast of the United States. *Mon. Wea. Rev.*, **118**, 324–342.
- Hein, P. F., and R. A. Brown, 1988: Observations of longitudinal roll vortices during arctic cold air outbreaks over open water. *Bound.-Layer Meteor.*, **45**, 177–199.
- Hodur, R., 1997: The Naval Research Laboratory's Coupled Ocean/Atmosphere Mesoscale Prediction System (COAMPS). *Mon. Wea. Rev.*, **125**, 1414–1430.
- Kelly, R. D., 1984: Horizontal roll and boundary-layer interrelationships observed over Lake Michigan. *J. Atmos. Sci.*, **41**, 1816–1826.
- Killworth, P. D., 1983: Deep convection in the world ocean. *Rev. Geophys. Space Phys.*, **21**, 1–26.
- Kristovich, D. A. R., 1993: Mean circulations of boundary layer rolls in lake-effect snow storms. *Bound.-Layer Meteor.*, **63**, 293–315.
- Kuettner, J., 1959: The band structure of the atmosphere. *Tellus*, **11**, 267–294.
- , 1971: Cloud bands in the earth's atmosphere: Observations and theory. *Tellus*, **23**, 404–425.
- Lab Sea Group, 1998: The Labrador Sea Deep Convection Experiment. *Bull. Amer. Meteor. Soc.*, **79**, 2033–2058.
- LeMone, M. A., 1973: The structure and dynamics of horizontal roll vortices in the planetary boundary layer. *J. Atmos. Sci.*, **30**, 1077–1091.
- Lilly, D. H., 1966: On the stability of Ekman boundary layer flow. *J. Atmos. Sci.*, **23**, 481–494.
- Martin, T., and S. Bakan, 1991: Airplane investigation of a case of convective cloud bands over the North Sea. *Bound.-Layer Meteor.*, **56**, 359–380.
- Miura, Y., 1986: Aspect ratios of longitudinal rolls and convection cells observed during cold air outbreaks. *J. Atmos. Sci.*, **43**, 26–39.
- Mourad, P. D., and R. A. Brown, 1990: Multiscale large eddy states in weakly stratified planetary boundary layers. *J. Atmos. Sci.*, **47**, 414–438.
- Reinsch, C. H., 1967: Smoothing by spline functions. *Numer. Math.*, **10**, 177–183.
- Renfrew, I. A., G. W. K. Moore, T. R. Holt, S. W. Chang, and P. Guest, 1999: Mesoscale forecasting during a field program: Meteorological support of the Labrador Sea Deep Convection Experiment. *Bull. Amer. Meteor. Soc.*, **80**, 605–620.
- Smith, S. D., 1988: Coefficients for sea surface wind stress, heat flux, and wind profiles as a function of wind speed and temperature. *J. Geophys. Res.*, **93**, 15 467–15 472.
- Sykes, R. I., W. S. Lewellen, and D. S. Henn, 1988: A numerical study of the development of cloud-street spacing. *J. Atmos. Sci.*, **45**, 2556–2569.
- Thiebaux, H. J., and M. A. Pedder, 1987: *Spatial Objective Analysis with Applications in Atmospheric Science*. Academic Press, 295 pp.
- Walter, B. A., 1980: Wintertime observations of roll clouds over the Bering Sea. *Mon. Wea. Rev.*, **108**, 2024–2031.
- , and J. E. Overland, 1984: Observations of longitudinal rolls in a near neutral atmosphere. *Mon. Wea. Rev.*, **112**, 200–208.
- Weckworth, T. M., J. W. Wilson, R. M. Wakimoto, and N. A. Crook, 1997: Horizontal convective rolls: Determining the environmental conditions supporting their existence and characteristics. *Mon. Wea. Rev.*, **125**, 505–526.